Supporting Information for

Unveiling the anomaly water uptake in concrete: Coupled pore evolution and swelling-induced crack closure

Hao Wang[1,2], Puttipong Srimook[3], Ryo Kurihara[1], Luge Cheng[1], Jiaping Liu[2], Ippei Maruyama[1,4,5] ✉

1 Department of Architecture, Graduate School of Engineering, The University of Tokyo, Tokyo, 113-8656, Japan

2 School of Materials Science and Engineering, Southeast University, Nanjing, 210098, China

3 Department of Civil Engineering, Faculty of Engineering, Rajamangala University of Technology Thanyaburi, Pathum Thani, 12110, Thailand

4 Department of Environmental Engineering and Architecture, Nagoya University, Nagoya, 464-8603, Japan

5 Green Cross-Tech Research Center, Tohoku University, Sendai, 980-8579, Japan

✉ E-mail: i.maruyama@bme.arch.t.u-tokyo.ac.jp

Table of Contents

List of Supplementary notes

Supplementary notes

Supplementary Note 1. Detail of drying process

An internal drying gradient in concrete has been cited as a potential cause of anomalous water uptake.[1, 2] Even after prolonged drying at 60 °C, a residual humidity gradient extending several tens of millimeters can persist.[3] To avoid this effect, concrete slices with dimensions of 100 × 100 × 10 (±1) mm³ were used in this study, ensuring uniform moisture distribution throughout the thickness.

Three drying regimes—20 °C, 60 °C, and 105 °C—were applied to produce specimens with varying degrees of dryness and distinct pore structure states. The 20 °C condition was controlled using a silica gel-based climate chamber, maintaining 20 ± 2 °C and 15 ± 3% RH. The 60 °C and 105 °C conditions were maintained using laboratory ovens with ±1 °C accuracy. Samples were considered to have reached mass equilibrium when mass loss was less than 0.03% over a 24-hour period. A schematic diagram of the drying procedure is shown in **Supplementary Figure 1a**.

The normalized mass loss curves and the corresponding equilibrium times are presented in **Supplementary Figure 1b**. Solid lines represent the average of at least four specimens; error bars indicate the standard deviation. As drying temperature increases, mass loss accelerates, equilibrium is reached sooner, and final water loss increases significantly. This is attributed to enhanced evaporation from small pores at elevated temperatures, leading to the removal of both gel water and a portion of chemically bound water.[3, 4] After 120, 696, and 1020 hours of drying, final water losses of 2.74%, 5.37%, and 6.25% were observed for the 20 °C, 60 °C, and 105 °C samples, respectively.

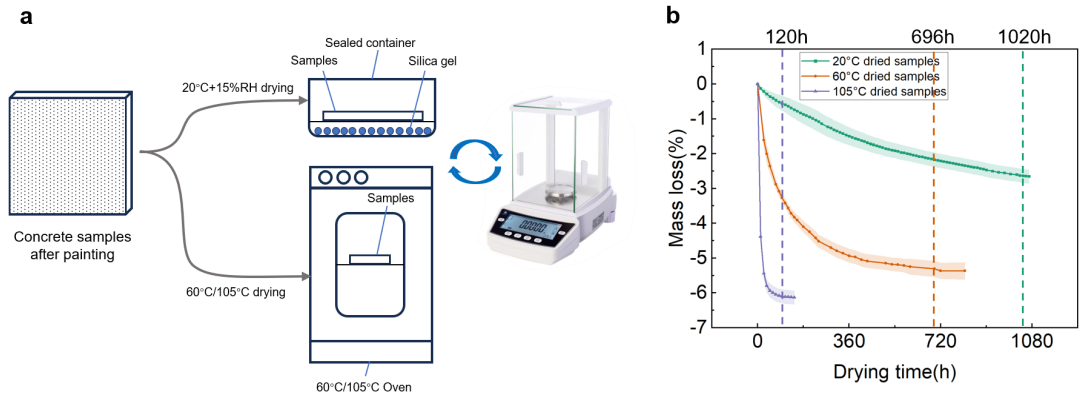

Supplementary Figure 1. Drying process and mass loss.
a Schematic of the drying protocols under three conditions: 20 °C at 15% RH (silica-gel chamber), 60 °C (oven), and 105 °C (oven).
b Normalized mass loss curves over time, showing the drying kinetics and the time required for each condition to reach mass equilibrium. Error bars represent standard deviation across at least four replicates.

Supplementary Note 2. X-CR test procedure and water content calculation method.

As illustrated in Fig.1 of the main manuscript, the concrete slice specimen was placed in the central chamber of the X-CR system. Each sample rested on a plastic base, allowing its underside to be exposed. Water was added to a surrounding reservoir until the level reached approximately 3–5 mm above the bottom surface—consistent with standard immersion protocols.[5, 6, 7, 8] A schematic of the setup, including physical dimensions and configuration, is shown in **Supplementary Figure 2a**. Throughout the CIC, DIC, and X-CR experiments, the same water absorption procedure was applied. The water level was checked and replenished every 8 hours to ensure constant immersion depth.

Due to equipment constraints, the X-ray observation window was limited to a 50 × 100 mm² region in the middle of the specimen, as shown in **Supplementary Figure 2b** . The attenuation of X-ray intensity follows the Beer–Lambert law. The water content at each pixel was calculated following the method of Roels and Carmeliet[9] using Equation (1):

$$\Delta C_w \cdot \mu_w = -\frac{\rho_w}{d} \ln \frac{I_{wet}}{I_{dry}} \qquad (1)$$

where I_{wet} and I_{dry} are the attenuated X-ray intensities for wet and dry specimens, respectively; ρ_w is the density of water (g/cm^3), d is the thickness of water (cm), and μ_w is the nominal attenuation coefficient of water in the sample (cm^{-1}).

In order to investigate the water content distribution, d=1cm and ρ=1g/cm^3 were used in Eq. (1). The relationship between mass change and $-\frac{\rho_w}{d} \ln \frac{I_{wet}}{I_{dry}}$ was linearly fitted to calculate μ_w, as shown in **Supplementary Figure 2c**. The resulting value of μ_w was 0.0133 cm^{-1}. A small y-intercept (−0.00005) in the fitted curve arises from the exclusion of grayscale changes in the submerged zone, but this has negligible impact on the accuracy of the slope.

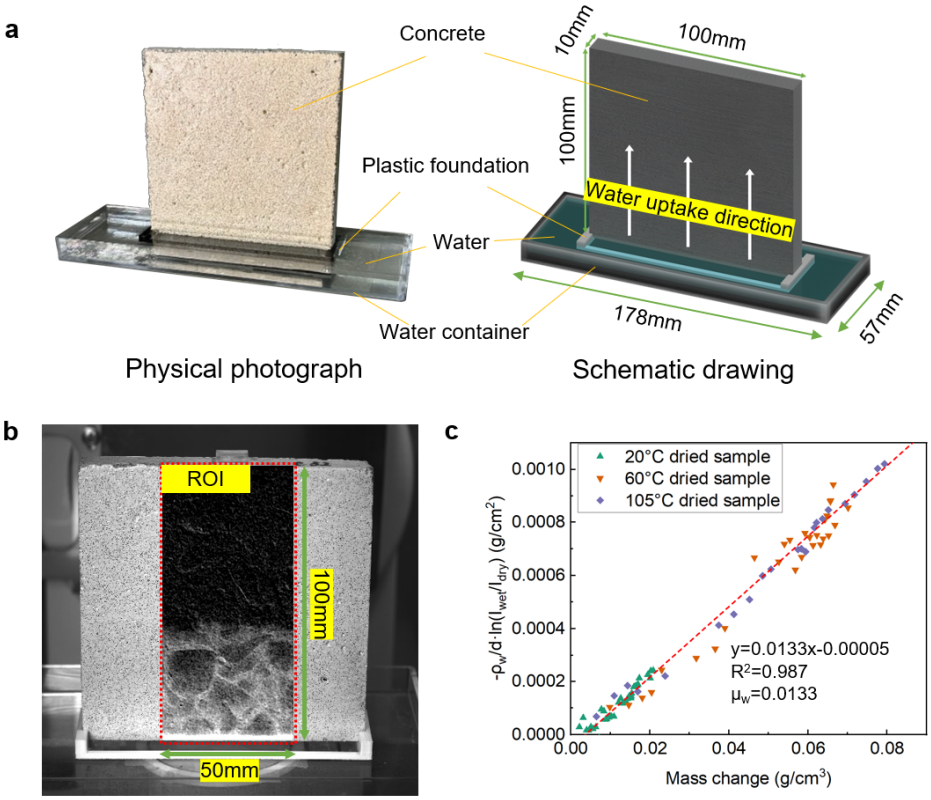

Supplementary Figure 2. Additional information on the X-CR test setup and grayscale calibration.

a Dimensions and configuration of the water uptake test setup, including concrete sample, plastic support base, and water container. The left image shows a physical photograph; the right is a schematic illustrating immersion depth and water uptake direction.

b Image of a representative sample during testing, with the region of interest (ROI) for X-CR analysis

indicated.
c Calibration curve showing the linear relationship between grayscale change and mass gain for samples dried at 20 °C, 60 °C, and 105 °C. All data follow a consistent slope of 0.0133 cm^{-1}.

Supplementary Note 3. NMR setup, testing protocol, and data processing.

Single-sided NMR was employed due to its minimal constraints on specimen size, making it suitable for dynamic water uptake tests on large samples. By translating the bottom magnet, the system generates a movable magnetic field, allowing repeated signal acquisition at a fixed height.[10, 11, 12] In this study, water content and its evolution at a height of 8 mm were monitored dynamically by repeatedly scanning a fixed test layer, thereby avoiding the long acquisition time required for full-depth profiling.[13, 14] The specimen dimensions were 50 × 50 × 100 mm^3, and the effective sampling volume was ~40 × 40 × 0.2 mm^3 in the specimen center. The test setup is shown in **Supplementary Figure 3**a , and an example of the signal decay curve after 36 h of water uptake at 60 °C is shown in **Supplementary Figure 3**b.

Although inverse Laplace transformation (ILT) is widely used for NMR data interpretation due to its ability to resolve peak positions and intensities,[15, 16] it requires a high signal-to-noise ratio (S/N), typically exceeding 150.[12] This demand is not compatible with the time-sensitive nature of dynamic absorption tests. Therefore, the CPMG decay at each time point was fitted using a bi-exponential function, as shown in Equation (2):

$$S(t)=A_1 e^{(-t/T_{2,1})}+A_2 e^{(-t/T_{2,2})} \quad (2)$$

where $S(t)$ is the magnetization at time t; A_1 and A_2 are the amplitudes corresponding to relaxation times $T_{2,1}$ and $T_{2,2}$, respectively. These components represent water in fine pores (e.g., interlayer and gel pores) and coarse pores (e.g., capillary and interhydrate voids), respectively.[17, 18]

A reference sample containing 6 mM $CuSO_4 \cdot 5H_2O$ was tested under identical conditions. Its decay curve was fitted using a mono-exponential function (Equation 3):

$$S_{ref}(t)=A_{ref} e^{(-t/T_{2,ref})} \quad (3)$$

The volumetric water content (w) in each pore category at any given time point was quantified by normalizing A_1 and A_2 of the concrete sample to A_{ref} of the copper sulfate solution.

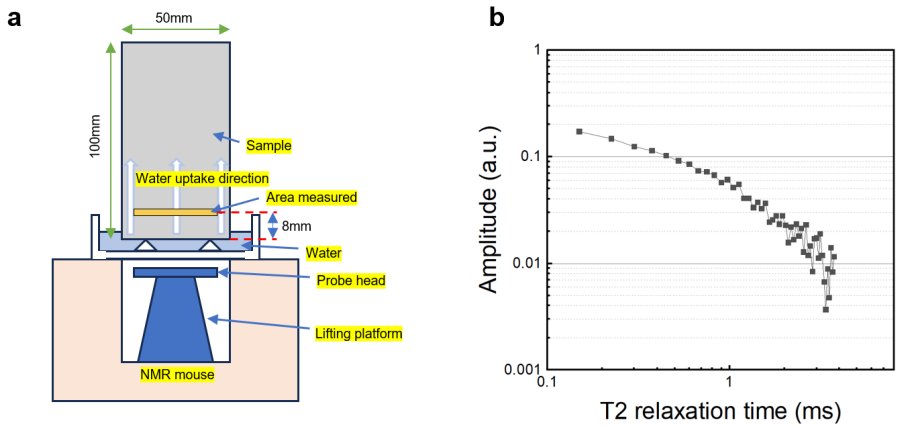

Supplementary Figure 3. Schematic and signal response of single-sided ^{1}H-NMR test.
a Experimental setup including the NMR device, concrete specimen dimensions (50×50×100 mm^3), and the defined test region (~40×40×0.2 mm^3) centered at 8 mm from the specimen base.
b Representative signal decay curve of the CPMG sequence for a specimen dried at 60 °C, measured after 36 h of water uptake.

Supplementary Note 4. Trends in NMR data and macropore compression from T_2 relaxation behavior.

The initial water content varied significantly among samples subjected to different drying conditions, as reflected by the first time-point measurements in **Supplementary Figure 4a-c**. With increasing drying temperature, the initial water content at a height of 8 mm was approximately 0.045 g/cm³ (20 °C), 0.023 g/cm³ (60 °C), and 0.011 g/cm³ (105 °C), respectively. Following water contact, the water content at 8 mm rose sharply after ~1.12 $h^{0.5}$ (20 °C), ~0.85 $h^{0.5}$ (60 and 105 °C), and reached a plateau at ~4, 2, and 2 $h^{0.5}$, respectively. The final plateau water content showed a slight increasing trend with higher drying temperature.

In specimens dried at 20 °C, capillary narrowing induced by C-S-H swelling is not readily observable due to the limited capillary volume and near-zero water content in these pores. Most absorbed water is directly retained in finer pores. At 60 °C, water initially fills capillary and fine pores in nearly equal proportions, followed by redistribution[19]—water migrates from capillaries into fine pores, concurrent with pore constriction caused by C-S-H swelling. This redistribution persists throughout the test. For specimens dried at 105 °C, approximately 60% of water initially enters capillary pores, with gradual redistribution into finer pores occurring later. After ~11 $h^{0.5}$, water content in both pore types converges, followed by continued redistribution.

These observations confirm two important mechanisms: (1) water redistribution significantly alters the internal pore structure, and (2) higher drying temperatures coarsen the pore network, making it less responsive to C-S-H-induced compression. Most notably, the delay and suppression of anomalous water uptake at elevated drying temperatures are directly linked to reduced pore constriction due to structural insensitivity.

Supplementary Figure 4d shows the evolution of T_2 relaxation times in capillary pores for the 60 °C and 105 °C conditions (with data gaps due to equipment maintenance). Data from 20 °C samples are omitted due to insufficient signal strength in capillary pores. The prolonged high-T_2 signal retention at 105 °C indicates that larger pores remain open longer, thereby sustaining high initial water uptake rates and delaying the onset of anomalous behavior.

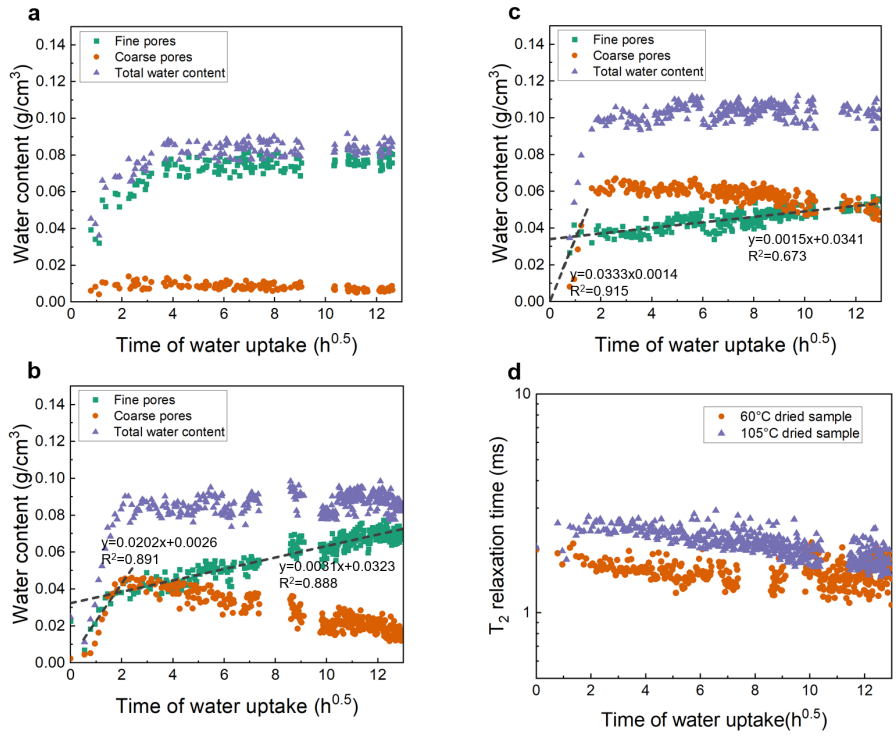

Supplementary Figure 4 Detailed visualization and extension of NMR data.
a–c Time-resolved evolution of water content in capillary and fine pores during water uptake for samples dried at 20 °C, 60 °C, and 105 °C. Gaps in the curves are due to temporary suspension of NMR scanning during instrument maintenance; water absorption continued uninterrupted during these

periods.
d Variation in T_2 relaxation times of capillary pores as a function of water uptake time for the 60 °C and 105 °C samples. Data for the 20 °C condition are excluded due to insufficient NMR signal resulting from minimal capillary water content.

Supplementary Note 5. Microstructural changes induced by drying: BSE image analysis and crack quantification

5.1 Experimental setup and image processing

Drying-induced pore coarsening has been widely reported in the literature.[20, 21] This phenomenon is primarily attributed to the consolidation of globular C–S–H clusters driven by surface free energy minimization. In addition to pore enlargement, severe drying can also result in microcracking due to autogenous restraint, especially in the presence of aggregates. These cracks and coarsened pores increase the permeability of concrete[22, 23], facilitating the transport of water and aggressive agents. [24]

To evaluate the evolution of porosity and microstructural damage—particularly at the capillary scale, which dominates liquid water transport—concrete specimens (100×10×100 mm³) were subjected to varying drying regimes and subsequently analyzed by backscattered electron (BSE) imaging. Specimens were polished and coated with 15 nm of carbon using a VC-100 carbon coater (Vacuum Device, Japan). Imaging was conducted using a JEOL JSM-7800F scanning electron microscope under vacuum at 15 kV and a working distance of ~5.0 mm.

Porosity and cracking were statistically analyzed across magnifications ranging from 50× to 1000×. Grayscale images were processed using MATLAB 2024a. K-means clustering was applied for threshold segmentation of pore and solid phases (**Supplementary Figure 5a**). Cracks were identified based on morphological parameters—specifically area and circularity—and manually reviewed to ensure reliability. For statistical robustness, over 12 images were analyzed per magnification and drying condition, with a total of more than 20000 cracks identified.

5.2 Qualitative comparison of crack development

BSE images at 500× magnification (**Supplementary Figure 5b**) reveal the development of microcracks under different drying conditions. At 20 °C, dense matrix structure is observed, with sparse cracks appearing along portlandite (regions A and C) and limited propagation around aggregates (region B). These cracks are isolated and poorly connected.

In contrast, samples dried at 60 °C show a higher density of matrix cracks, with some forming connected pathways through the matrix (regions D–G), potentially serving as preferential transport channels. At 105 °C, crack morphology shifts toward fewer but larger, more continuous cracks (regions H and J), likely caused by rapid drying and associated energy release. These wide cracks may connect interfacial transition zones between aggregates, forming dominant pathways for water transport.

5.3 Quantitative crack geometry analysis

Three parameters—crack length (L), area (A), and average width (W = A/L)—were used to quantify individual cracks. Statistical results from >450 BSE images at varying magnifications are presented in **Supplementary Figure 6a-c**.

Most cracks had lengths between 1–100 μm, peaking around 10 μm. With increased drying temperature, longer cracks became more frequent, though cracks near 100 μm showed limited growth beyond 60 °C (**Supplementary Figure 6a**). Crack areas ranged from 0.1–1000 μm², with 60 °C drying promoting a shift from small (0.1–10 μm²) to medium (10–1000 μm²) cracks (**Supplementary Figure 6b**). Further heating to 105 °C primarily widened existing cracks. Crack widths spanned 0.1–10 μm and increased consistently with temperature across all scales (**Supplementary Figure 6c**).

Porosity also increased with both magnification and drying severity (**Supplementary Figure 6d**). The effect of drying-induced coarsening was more pronounced at higher magnifications, indicating stronger changes at finer pore scales. At 50×, porosity deviated from

the trend due to aggregate and air void interference in the larger field of view.

To further describe cracking behavior, two normalized parameters[25] were introduced: areal fraction (A_a) and crack density (L_a), calculated by:

$$A_A = \frac{1}{A} \sum_{k=1}^{n} (A_k) \quad (4)$$

$$L_A = \frac{1}{A} \sum_{k=1}^{n} (L_k) \quad (5)$$

where A is the area of the observation window, A_k and L_k are the area and length of individual cracks, and n is the total number of cracks.

Crack quantity at 60 °C and 105 °C was significantly higher than at 20 °C under 50–500× magnification (**Supplementary Figure 6e**). At 1000×, differences diminished due to the small observation window. Crack quantity peaked at 100×, suggesting it as an optimal scale for bulk crack quantification.

Crack density generally increased with both magnification and drying severity (**Supplementary Figure 6f**). A rightward shift in the probability distribution of crack area fraction (Figure 6g) confirmed that higher drying temperatures produced more large-area cracks, with 105 °C showing the greatest fraction of cracks exceeding 1% of the observation area.

5.4 Correlation with water uptake and deformation

Porosity was found to correlate linearly with the initial water uptake rate (**Supplementary Figure 6h**). To compare porosity across scales, values were normalized against the porosity of 105 °C-dried samples. Error bars represent variability across magnifications.

Figure 6i displays the post-drying deformation field, consistent with previous reports.[26] Low-deformation zones coincide with aggregate-rich regions, while high-strain zones (>2000 μm/m) correspond to matrix areas. Extreme strains (-5000 μm/m) may indicate microcrack clusters.

Importantly, the transport phenomena described here differ from water flow through visible macrocracks.[27, 28, 29, 30] No through-cracks were observed in this study. Instead, deformation and transport are governed by localized microcrack networks, typically below 10 μm in width (**Supplementary Figure 6c**), which subtly enhance water migration without forming visible channels.

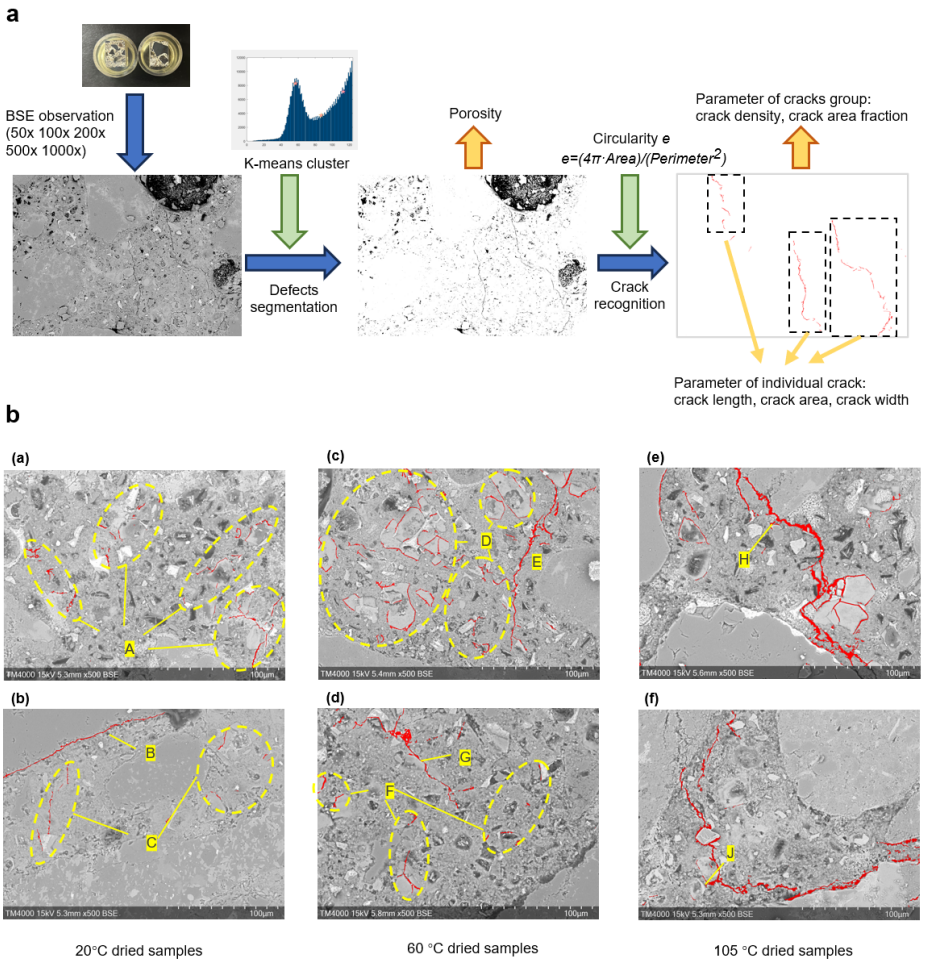

Supplementary Figure 5. BSE imaging and statistical analysis of capillary structure and microcrack development.
a Workflow for BSE image acquisition and quantitative analysis. Individual crack parameters—including length, area, and width—were extracted alongside group metrics such as crack density and areal fraction.
b Comparison of microcrack morphology under different drying conditions using BSE images at 500× magnification. (a–b) 20 °C-dried sample; (c–d) 60 °C-dried sample; (e–f) 105 °C-dried sample. Regions of interest illustrate typical crack patterns and their spatial distribution.

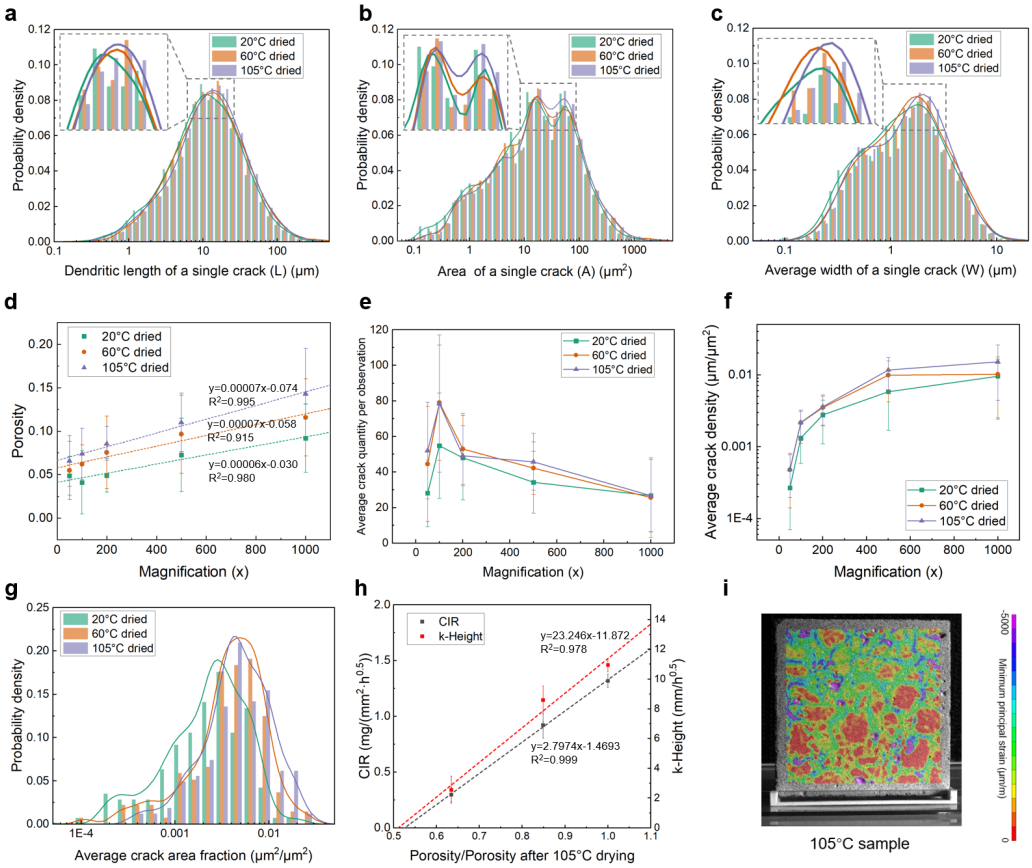

Supplementary Figure 6. Quantitative analysis of crack geometry, porosity, and their correlation with water uptake and strain.
a–c Statistical distributions of individual crack parameters—length, area, and width—for samples under 20 °C, 60 °C, and 105 °C drying conditions. Insets highlight regions near the distribution peaks.
d Relationship between measured porosity and image magnification. Dashed line represents a linear fit.
e–f Mean number of cracks per image and crack density plotted as a function of magnification for each drying condition.
g Probability distribution of average crack area fraction, used as a key indicator of crack size across drying conditions.
h Correlation between relative porosity (normalized to 105 °C sample) and the initial water absorption rate (CIR/k-Height). Dashed lines show linear fits.
i Distribution of minimum principal strain after drying (105 °C sample). Low-strain regions correspond to aggregate zones, while moderate strain (-5000 μm/m, shown in purple) indicate microcrack clusters. No visible through-cracks were detected; these zones reflect localized accumulation of sub-visible microcracks, consistent with the characteristic width (a few microns) shown in panel **c**.

Supplementary Note 6. Microscale consequences of drying and their influence on the pre-anomalous water uptake phase.

The effect of drying temperature on the pore structure evolution has been previously investigated by our group. [20, 23] Here, based on the statistical porosity data (from BSE analysis) and real-time NMR observations during water uptake, we further elucidate the drying-induced microstructural transformations and their implications for early-stage absorption dynamics. A conceptual schematic is provided in **Supplementary Figure 7** to visualize the changes.

20 °C + 15%RH (mild drying):

Even under relatively mild conditions, capillary water and most gel water are effectively removed, and C-S-H gel undergoes partial consolidation. The formerly amorphous gel acquires

a more fibrous morphology. Capillary pores are sparsely distributed, poorly connected, and contribute little to macroscopic water transport. As a result, porosity observed by BSE is low, and water uptake at this stage is limited.

During re-immersion, remaining gel pores are easily refilled, but the rehydrated C–S–H matrix cannot accommodate further water ingress. Interlayer water remains largely intact, and thus water redistribution does not occur significantly, unlike the higher-temperature-dried samples.

60 °C (moderate drying):

At 60 °C, consolidation of C–S–H clusters progresses further, including partial transformation of needle-like phases. Larger pore sizes and newly formed transport channels between adjacent capillary pores contribute to a marked increase in total porosity and enhanced water conductivity.

At the gel scale, all gel water and some interlayer water are removed. Some C–S–H layers collapse and bond via intermolecular forces, reducing pore volume. Simultaneously, weaker layers are pulled apart, generating new gel-scale pores. This dual behavior—collapse and expansion—produces a more complex pore network.

105 °C (severe drying):

The structural changes at 105 °C follow a similar pattern to those at 60 °C but are more pronounced. Total porosity is further increased, and capillary pore networks become nearly continuous. NMR data show that, compared to 60 °C, more gel regions are rapidly re-filled during initial absorption, indicating more readily accessible gel-scale pores due to severely delaminated interlayer spaces.

However, water redistribution within the matrix is slower and more restricted. This is attributed to tighter bonding between consolidated C-S-H layers, which limits the re-absorption of water into deeper gel and interlayer regions.

Summary:

The consolidation and morphological rearrangement of C–S–H gel during drying critically influence the pore network and its functionality. With increased drying severity:

- Capillary pore volume and connectivity increase;
- Gel pore accessibility improves, favoring faster initial absorption;
- Tightly packed interlayer structures hinder later redistribution.

This drying-induced asymmetry between capillary inflow and redistribution contributes to the onset and modulation of anomalous water uptake behavior in cementitious materials.

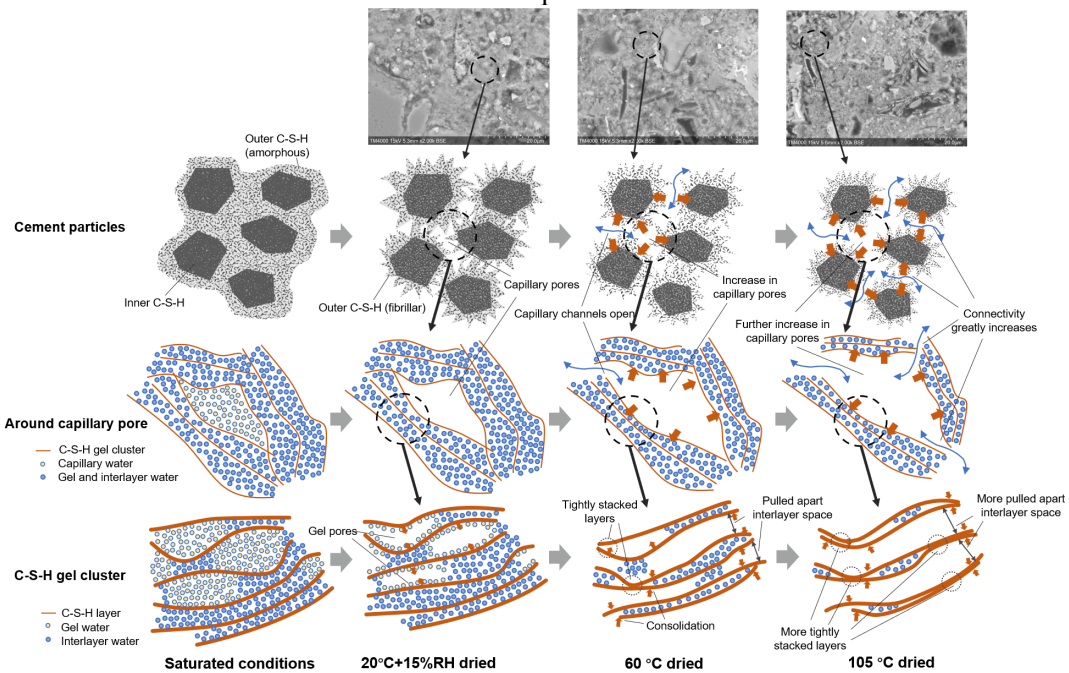

Supplementary Figure 7 Schematic representation of microstructural changes at multiple scales after

different drying conditions.
Conceptual illustration of the morphological evolution of cement particles, capillary pores, and C-S-H gel globules under 20 °C, 60 °C, and 105 °C drying regimes. The figure highlights changes in pore connectivity, gel densification, and interlayer spacing that collectively influence water accessibility and transport behavior. Note: this is a schematic depiction and not based on actual microscopy images.

Supplementary Note 7. Determination method for penetration/expansion height.

While numerous studies have documented water distribution profiles during capillary uptake and proposed methods to quantify penetration height over time, a fundamental challenge lies in selecting consistent criteria for defining the boundary of penetration—especially when a transition zone is present. Based on strain and water content distributions, the specimen can be conceptually divided into three regions: fully saturated, partially filled, and dry. These regions respectively correspond to zones of maximum, intermediate, and negligible expansion or water content, as illustrated in **Supplementary Figure 8a**.

Notably, the "fully saturated" region may not exhibit 100% pore filling. In prior studies, the accessible pore volume in mortars with water–cement ratios of 0.6 and 1.15 reached only ~55.7% and ~60.6%, respectively.[31] Moreover, the residual unfilled pores in saturated zones and the extent of the transition zone—also referred to as the "wetting front composite region"—increase with pore structure heterogeneity, a common characteristic in porous materials.[32] This observation challenges the assumptions of the classic Lucas–Washburn (L–W) model and supports the possibility of anomalous water uptake behavior.

The transition zone, which typically contains large pores and strong gradients in saturation or strain, can be bounded by two critical positions: the height of the beginning (A) and end (B) of the transition zone can be easily recognized, as shown in **Supplementary Figure 8**a.

While point A underestimates and point B overestimates the true penetration height, an intermediate compromise is the intersection point C, defined as the intersection between tangents drawn along the steep gradient and the plateau. This method is often used in setting-time analysis for cementitious systems.[33]

However, when strain or water content profiles are noisy or nonlinear—such as in this study—the tangent-based method becomes ambiguous. Therefore, we adopt point D, defined as the position where the water content or strain equals the arithmetic mean of the fully saturated and dry regions. This method offers simplicity, reproducibility, and computational efficiency, and was found to approximate point C with reasonable accuracy.

To capture lateral variations in water uptake, the specimen's surface is divided into eight horizontal strips (see **Supplementary Figure 8b**), and the penetration height is calculated separately for each strip. This approach improves spatial resolution and follows recommendations in Refs.[34, 35]

Supplementary Note 8. Temporal evolution of saturated, transition, and dry zones during water uptake.

Supplementary Figure 8c-h present the evolution of distinct moisture and deformation regions over time for specimens under different drying conditions. In all cases, the penetration height increases with time and is positively correlated with the drying temperature, indicating enhanced absorption capacity in more severely dried samples.

Although a transitional zone is present in each sample, its relative thickness remains small compared to the total uptake height, suggesting that the wetting front is relatively sharp. Notably, the transition zone estimated from DIC-derived strain data is typically broader than that derived from X-CR-based moisture profiles. This discrepancy likely results from the elastic coupling effect of the material: deformation in the saturated region may propagate slightly into the dry zone, inducing minor strain responses even in areas not yet filled with water.

In addition, as shown by the mass uptake data, minor differences in water absorption kinetics were observed between replicate specimens under identical drying conditions. These inter-sample variations contribute to small discrepancies in the penetration height evolution

recorded by X-CR and DIC techniques.

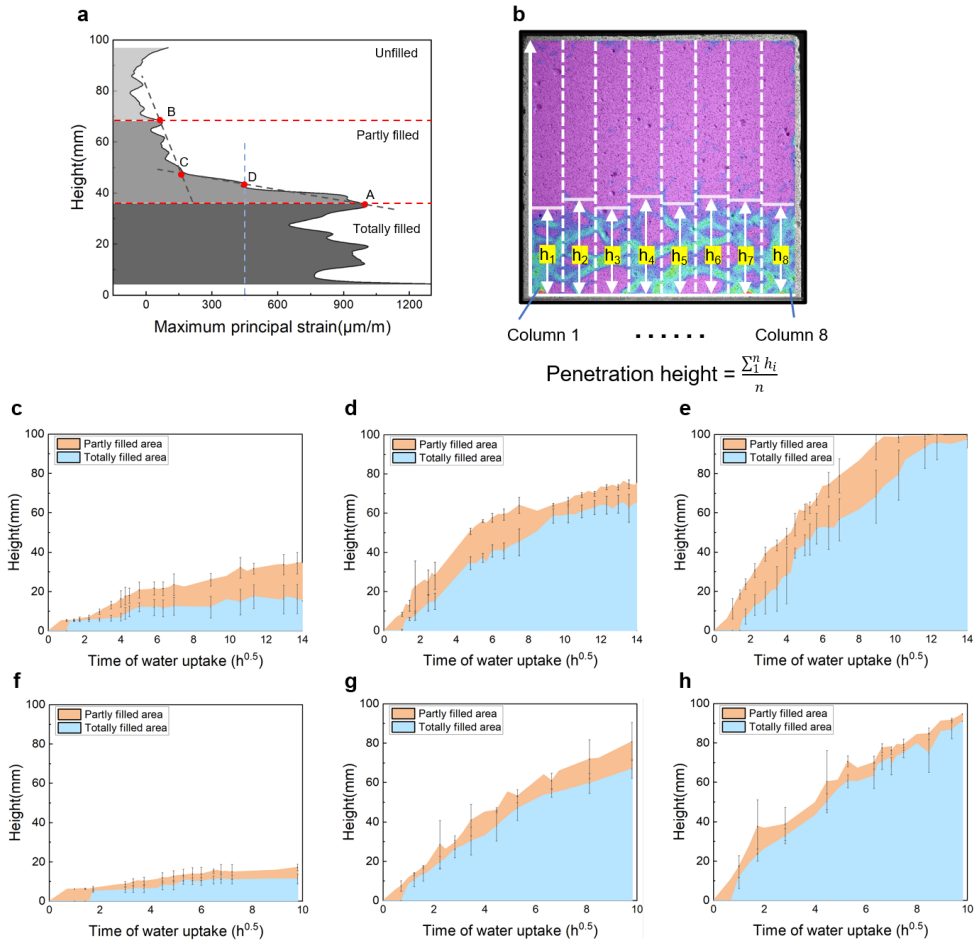

Supplementary Figure 8 Regional classification of water uptake and strain, and methods for penetration height determination.
a Typical water content and deformation profiles along the specimen height, showing the division into fully saturated, partially saturated, and dry zones. Points A–D represent different criteria for estimating the water penetration height.
b Illustration of the sectioning approach, where the specimen surface is divided into horizontal strips for independent calculation of penetration height. The associated formula for computing average height is also shown.
c–e Temporal evolution of fully expanded and partially expanded regions derived from DIC data for samples dried at 20 °C, 60 °C, and 105 °C, respectively.
f–h Temporal evolution of fully saturated and partially saturated regions derived from X-CR data for samples under the same drying conditions.

Supplementary Note 9. Relationship between penetration height and mass recovery.

Following an initial stage of rapid water uptake, the mass gain of dried specimens tends to stabilize and shows limited further increase. Although some studies suggest that additional water absorption may occur over extended timescales,[36, 37, 38] the relationship between final penetration height and mass recovery remains a valuable indicator of pore accessibility and rehydration capability.

As shown in **Supplementary Figure 9**, samples dried at 60 °C and 105 °C exhibit significantly lower mass recovery compared to 20 °C-dried specimens, even when the penetration height reaches comparable values. Under 20 °C drying, despite a low ambient relative humidity (15%), the mass lost during drying is almost completely regained in the saturated region. In contrast, for samples dried at 60 °C and 105 °C, the penetration height and

mass recovery ratio exhibit a near-linear relationship that deviates substantially from the ideal 1:1 line (red dashed line), indicating that roughly 50% of the lost water cannot be recovered.

Previous studies have shown that post-absorption water content remains well below the vacuum-saturated levels,[31] and recovery ratios are typically reported in the range of 60–90%. [39] This may be because some large voids trap air. This trapped air is thought to be approximately evenly distributed in the system and can sometimes be directly observed by visualizing water content profiles. Another possible explanation is that a large number of irreversibly closed hydrogel pores caused by heating and drying lead to this result. The present results favor the second hypothesis: samples subjected to mild drying (20 °C) exhibit minimal irreversible effects, achieving nearly complete mass recovery. By contrast, high-temperature-dried specimens display significant unrecoverable porosity, suggesting that irreversible gel pore closure is the dominant mechanism limiting water regain under these conditions.

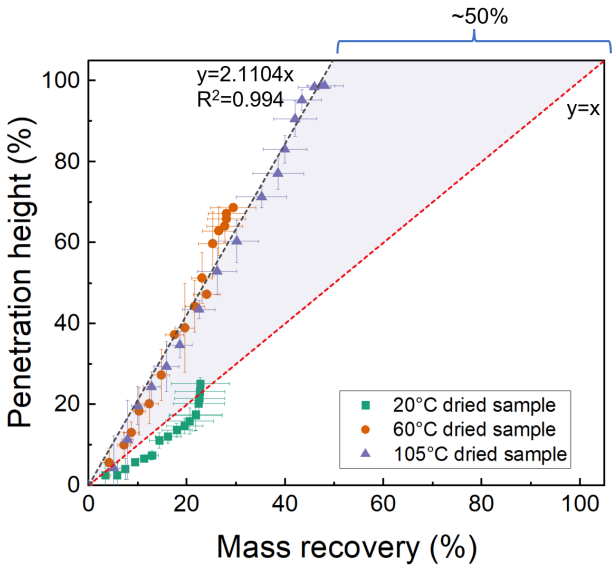

Supplementary Figure 9. Relationship between normalized penetration height and mass recovery ratio.
Scatter plot showing the correlation between the percentage of penetration height (normalized to specimen height) and the corresponding mass recovery ratio after water uptake for samples dried at 20 °C, 60 °C, and 105 °C. The red dashed line indicates the ideal 1:1 relationship, where all mass lost during drying would be fully recovered by water uptake. Deviations from this line illustrate the extent of unrecoverable water, particularly for samples subjected to higher drying temperatures.

Supplementary Note 10. Calculation of diffusion coefficient using the Boltzmann-Matano method.

With access to detailed time-resolved water content distributions during absorption, the Boltzmann–Matano method was employed to calculate the moisture-dependent diffusion coefficient D(θ). This method, originally proposed by Boltzmann[40] and further developed by Matano[41], has been successfully applied in water uptake studies of porous materials. [42] It transforms the time-dependent Fickian diffusion equation into a time-independent form, enabling the evaluation of D(θ) from concentration profiles at different times.
Starting from Fick's second law:

$$\frac{\partial \theta}{\partial t} = \frac{\partial}{\partial x}\left(D(\theta)\frac{\partial \theta}{\partial x}\right) \qquad (6)$$

By introducing the Boltzmann variable $\lambda = \frac{x}{\sqrt{t}}$, this partial differential equation is converted into:

$$\frac{d}{d\lambda}\left(D(\theta)\frac{d\theta}{d\lambda}\right) + \frac{1}{2}\lambda\frac{d\theta}{d\lambda} = 0 \qquad (7)$$

Here, θ(x, t) is the local moisture content, D(θ) is the effective diffusion coefficient, x is distance,

and t is time.

On the Matano interface (defined as the effective water front), D(θ) can be calculated through integration:

$$D(\theta) = -\frac{1}{\lambda}\int_{\lambda_M}^{\lambda}\frac{1}{2}\lambda\left(\frac{d\theta}{d\lambda}\right)d\lambda \quad (8)$$

Where λ_M is the position of the Matano plane.

The calculation procedure is illustrated in **Supplementary Figure 10**a:

Step I: Transform the water content profiles at each time point into θ(λ) using Boltzmann scaling.

Step II: Exclude the plateau zones (θ>0.08 g/cm³ and <0.01 g/cm³), and isolate the front region near the Matano plane.

Step III: Compute D(θ) from the θ(λ) curve using numerical integration. To reduce sensitivity to local fluctuations, the computed data are smoothed using an S-shaped fit near the front.

Step IV: Reconstruct θ(λ) from both the original and fitted D(θ), and compare results. Minor oscillations in D(θ) from raw data are attributed to noise in water content gradients but do not affect the overall trend or physical interpretation.

Supplementary Note 11. Position and evolution of the water front in Boltzmann coordinates.

Plotting water content θ(x, t) against the Boltzmann variable λ is a useful tool for identifying anomalous uptake behaviors (see **Supplementary Figure 10b-d**). When the water front propagates steadily, curves at different time points collapse onto a single profile in the θ(λ) domain.[43] In this representation, a steeper front indicates faster penetration.

Among the three drying conditions, 20 °C-dried samples exhibited the slowest water front progression. At early stages, the front is relatively diffuse, and water preferentially fills small capillary pores—evidenced by faster diffusion in the low-θ region.

As time progresses, the profile becomes steeper (Stage I), indicating accelerated filling of the pore network beneath the front. The onset of this rapid diffusion phase occurs at ~6 h for the 20 °C sample, and ~16 h for the 60 °C and 105 °C samples.

For the latter two cases, the water front stabilizes over a prolonged period (Stage II), maintaining a nearly constant gradient between 16–46 h (60 °C) and 16–64 h (105 °C). During this stage, the diffusion is balanced, and the front advances steadily. Although microstructural changes may occur behind the front, their impact on front progression remains minimal.

By contrast, the 20 °C sample exhibits no clear Stage II. It transitions directly to Stage III, where the water front movement slows down significantly despite a constant front shape—signifying the onset of anomalous uptake. This phase is marked by a substantial decline in water potential gradient and diffusion driving force.

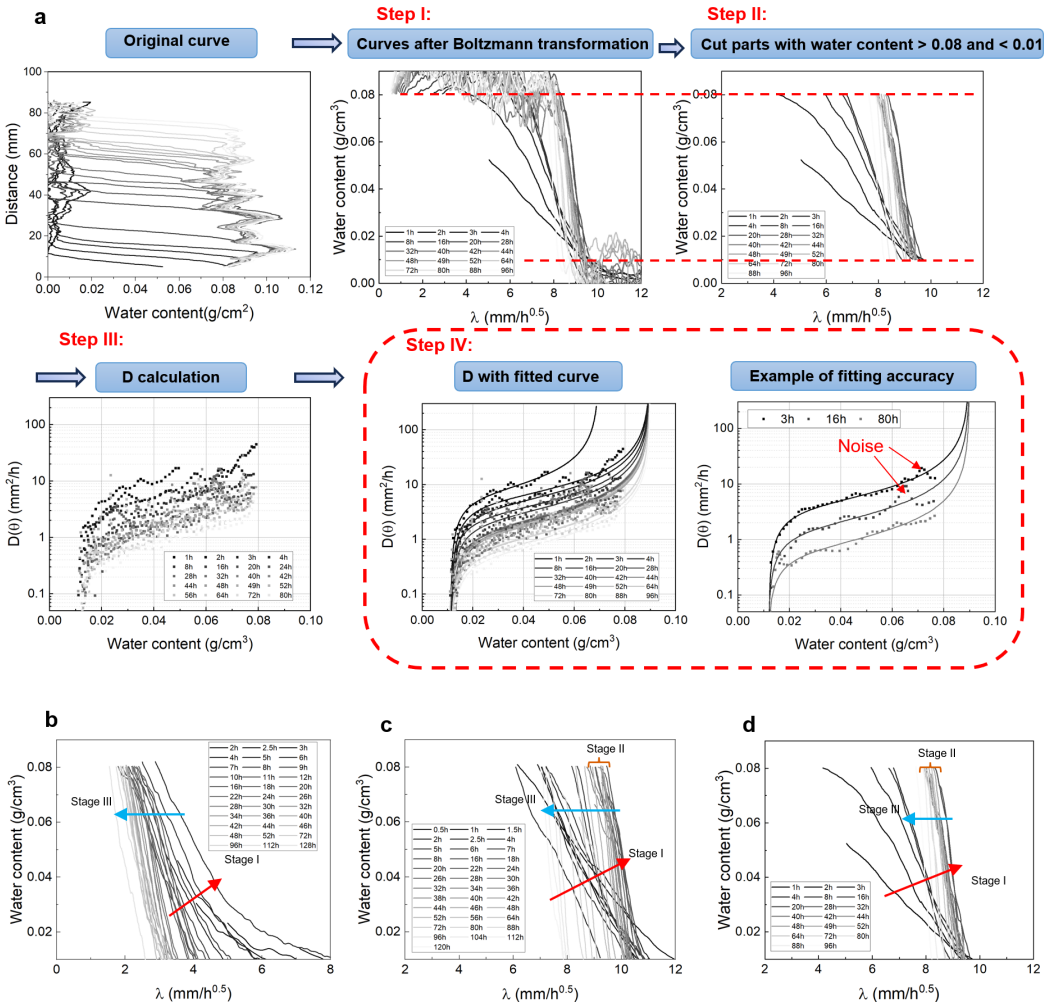

Supplementary Figure 10. Calculation of diffusion coefficient and intermediate results based on Boltzmann–Matano analysis.

a Flowchart of the diffusion coefficient computation process using Boltzmann–Matano transformation. The procedure is based on water content profiles along the absorption direction and includes four main steps: Boltzmann scaling, front isolation, numerical integration, and validation. **b–e** Intermediate results for specimens dried at 20 °C, 60 °C, and 105 °C. The plots show the moisture content θ as a function of the Boltzmann variable λ, used as the basis for extracting D(θ).

Supplementary Note 12. Explanation of the temporal mismatch between water content and volumetric expansion.

Based on synchronized X-CR and DIC measurements, a quasi-linear relationship can be observed between the average expansion across the specimen cross-section and the mean water content change, as shown in **Supplementary Figure 11**a. Among the three drying conditions, specimens dried at 20 °C exhibit the highest macroscopic expansion per unit water content, followed by 60 °C and 105 °C. This trend suggests that more dehydrated interlayer regions—present predominantly in mildly dried samples—correspond to greater swelling potential upon rehydration.

However, this average-based analysis masks the temporal discrepancy between local expansion and water content increase. **Supplementary Figure 11**b presents a direct comparison between the spatial distribution curves of water content and expansion at a given time. The DIC and X-CR profiles exhibit similar undulating patterns, reflecting the heterogeneous aggregate distribution across the cross-section. Despite minor spatial offsets, the peak positions of both curves align reasonably well in fully saturated regions. Dashed circles highlight representative

peak locations where intensity differences remain within a narrow range.

In contrast, within the transition zone, a clear mismatch emerges: the water content curve consistently surpasses the expansion curve in height, indicating a lag in mechanical response relative to fluid ingress.

This time-lag effect is further illustrated in **Supplementary Figure 11**c. A threshold water content value of approximately 0.05 g/cm³ (indicated by the dashed line) can be used to delineate the induction period—a regime during which water enters the structure but does not yet trigger significant macroscopic expansion. Once the local water content surpasses this critical value, volumetric strain increases markedly.

These observations confirm the existence of a two-phase expansion behavior and highlight the nonlinear coupling between water-induced swelling and fluid transport, particularly in partially saturated zones.

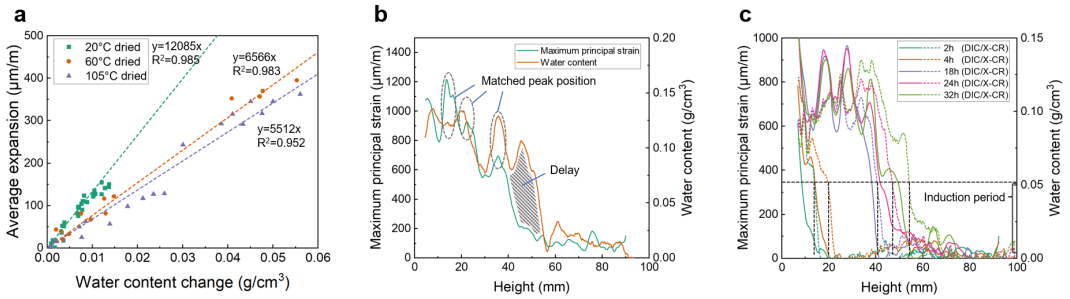

Supplementary Figure 11 Evidence of delay between water content increase and deformation onset from comparative DIC and X-CR analyses.
a Correlation between mean water content and average deformation across the region of interest (ROI).
b Comparison between water content and strain distribution curves for the sample dried at 60 °C after 24 h of water uptake. Dashed circles highlight aligned and misaligned peaks between the two curves.
c Determination of the threshold water content required to initiate macroscopic deformation, illustrated using the 105 °C-dried sample. The onset of expansion is identified relative to water content evolution.

Supplementary Note 13. Extended DIC and X-CR observations and corresponding distribution curves.

While the main manuscript presents the synchronized in-situ DIC and X-CR results for the 0–32 h period to enable direct comparison between water content and deformation, additional independent DIC and X-CR tests were performed to verify the anomalous water uptake behavior over extended durations. These results are shown in **Supplementary Figure 12**.

Supplementary Figure 12a-c display the evolution of the strain field in samples dried at 20 °C, 60 °C, and 105 °C, respectively. The corresponding deformation profiles along the specimen height are shown to the right of each field map. As water uptake time progresses, the height of deformation increases with drying temperature. For the 20 °C and 60 °C samples, deformation height plateaued after approximately 100 h, indicating that certain regions had reached complete saturation or had remained dry, a phenomenon that cannot be captured by mass-based measurements alone.

Supplementary Figure 12d-f present the water content evolution in samples under the same drying conditions. Water content distribution curves along the height are similarly provided. The trends in water penetration depth observed via X-CR closely match those seen in deformation height via DIC, confirming the consistency between mechanical and moisture field responses across different drying regimes.

These additional tests further support the reliability of the observed anomalous absorption characteristics and provide complementary spatial insights that bulk measurements cannot offer.

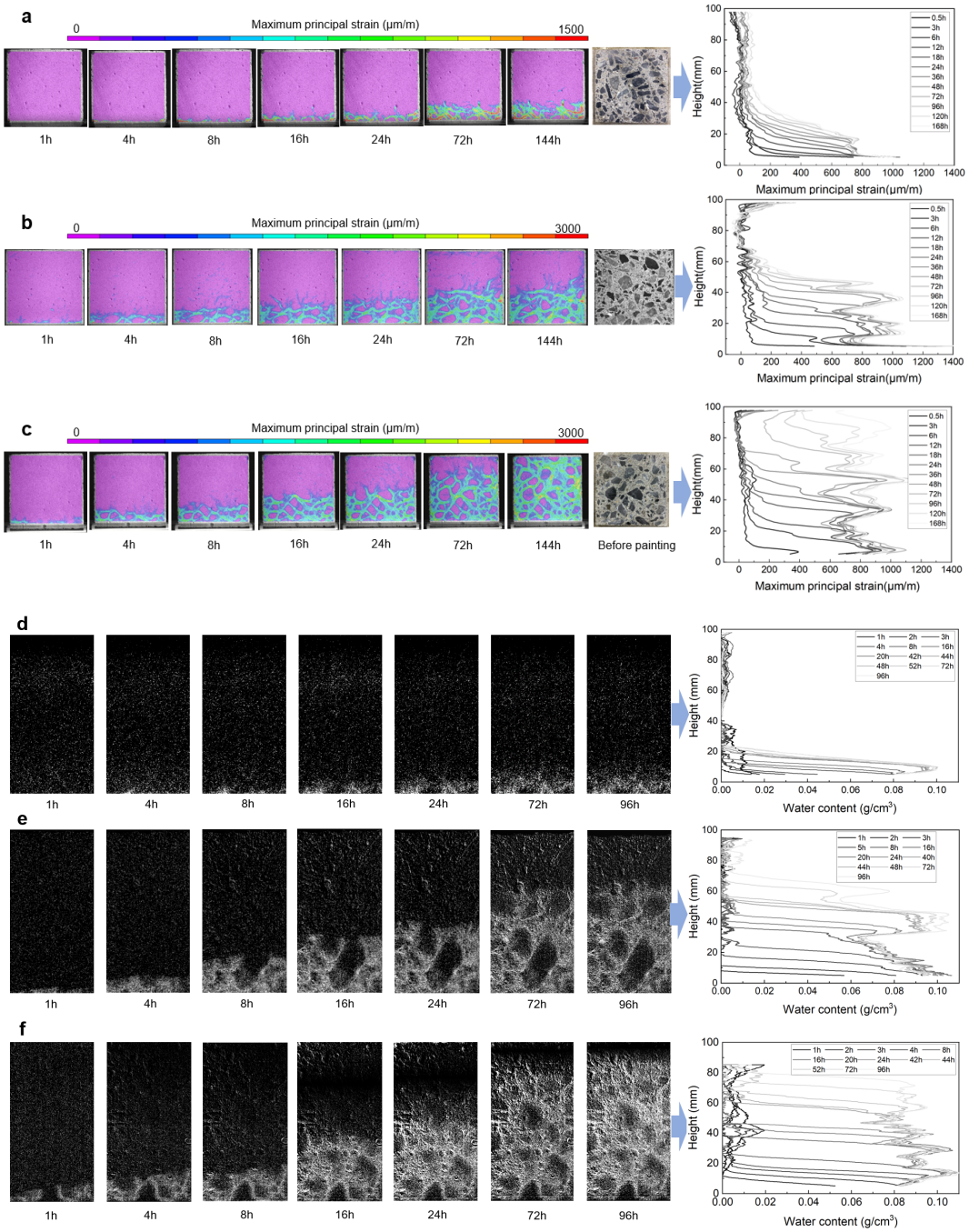

Supplementary Figure 12. Extended DIC and X-CR field maps and corresponding distribution profiles under different drying conditions.
a–c Maximum principal strain fields and vertical strain distribution curves for specimens dried at 20 °C, 60 °C, and 105 °C, respectively. Strain evolution is shown over the time range of 0–144 h.
d–f Water content field maps and corresponding height-wise water content distribution profiles over the period of 0–96 h for specimens under the same drying conditions. The spatial extent of moisture penetration is consistent with the deformation zone observed via DIC.

Supplementary Note 14. Evaluation of the $t^{0.25}$ time relationship for describing CIC evolution

Some fitting parameters in the manuscript are shown in **Supplementary Figure 13a-b**.**Supplementary Figure 13**c shows the results of repeated tests on water absorption quality. Although there is some dispersion, CIC under different drying conditions is still distinct.

Several previous studies[7, 8, 38, 44] have proposed that cumulative capillary water uptake (CIC) may follow a $t^{0.25}$ dependence, especially under anomalous absorption conditions. To evaluate this hypothesis, we re-plotted our CIC data against $t^{0.25}$ for samples dried at 20 °C, 60 °C, and 105 °C (see **Supplementary Figure 13d-f**). While the resulting plots do exhibit approximate linearity over intermediate time windows, the overall fitting performance raises several concerns.

First, the $t^{0.25}$ curves consistently exhibit a strong deviation from the origin, implying that this relationship fails to describe the early-time behavior (e.g., $t<1$ $h^{0.25}$). Second, although some individual samples (e.g., 20 °C-sample-2, 60 °C-sample-2, 105 °C-sample-1) appear to follow two-stage linearity, this pattern is not reproducible across all replicates, and a transition region is often observed that prevents a clean bilinear interpretation.

Moreover, using the $t^{0.25}$ formulation increases the dispersion of the extracted inflection points, particularly within the same drying condition. This undermines the consistency and predictability of the model.

Taken together, these results suggest that the $t^{0.25}$ scaling does not improve the description of CIC evolution compared to the classical $t^{0.5}$ relationship. In fact, our findings point to the broader conclusion that CIC behavior in anomalous regimes cannot be captured by a single power-law relationship, and may require more complex or piecewise models to fully characterize.

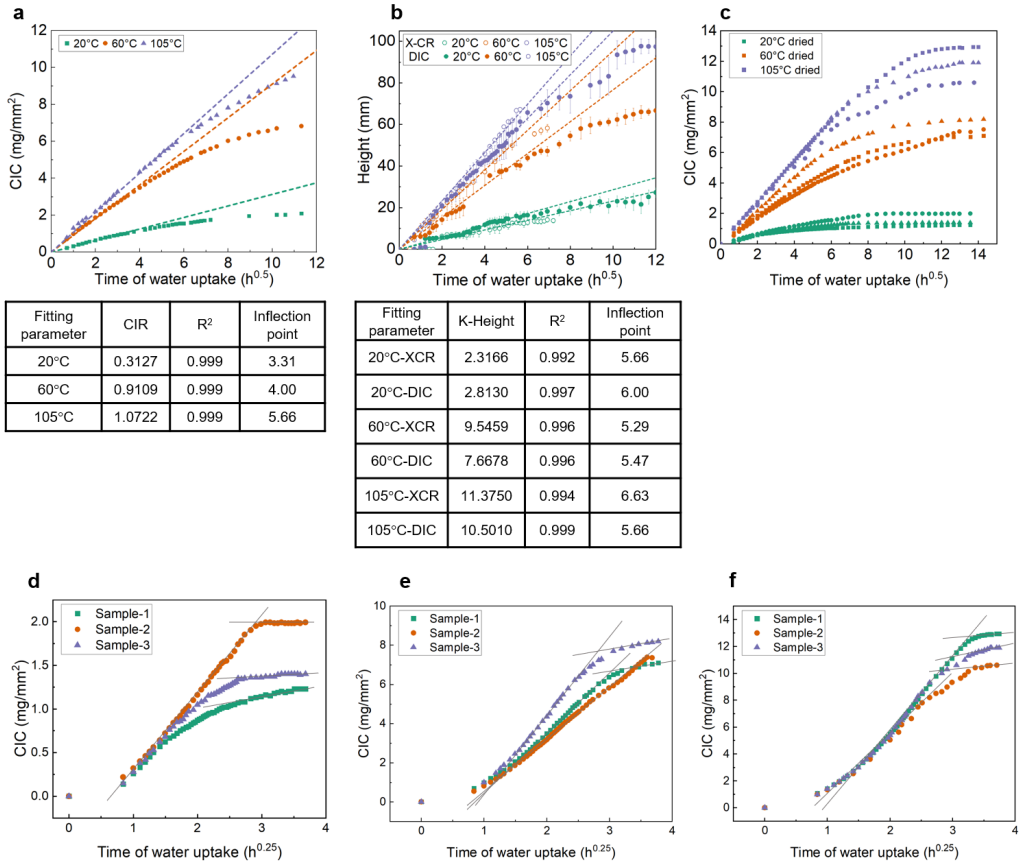

Fitting parameter	CIR	R^2	Inflection point
20°C	0.3127	0.999	3.31
60°C	0.9109	0.999	4.00
105°C	1.0722	0.999	5.66

Fitting parameter	K-Height	R^2	Inflection point
20°C-XCR	2.3166	0.992	5.66
20°C-DIC	2.8130	0.997	6.00
60°C-XCR	9.5459	0.996	5.29
60°C-DIC	7.6678	0.996	5.47
105°C-XCR	11.3750	0.994	6.63
105°C-DIC	10.5010	0.999	5.66

Supplementary Figure 13 Curve-fitting parameters related to anomalous water uptake behavior and repeatability of mass absorption measurements.
a CIC values and associated fitting parameters (e.g., initial slope, inflection point) derived from linear fits of the mass uptake curves, as presented in the main text.
b Corresponding results based on water uptake height derived from X-CR measurements, showing the relationship between penetration height and derived kinetic parameters.
c Results of repeated mass uptake tests for specimens dried at 20 °C, 60 °C, and 105 °C, illustrating the degree of experimental dispersion across replicates.

d–f CIC plotted as a function of $t^{0.25}$ for samples under the three drying conditions. While an approximate linear trend is observable in intermediate time ranges (highlighted by grey guide lines), all curves exhibit significant deviation from the origin, particularly at early times, suggesting limitations in the applicability of the $t^{0.25}$ model for anomalous absorption scenarios.

Supplementary Note 15. Assessment of gravitational effects on water uptake behavior.

Although the classical Lucas–Washburn (L–W) equation indicates that gravity has a negligible influence on capillary water uptake in materials with small characteristic pore sizes, recent studies[45, 46] still makes us worry that gravity is a disturbing factor for anomalous water uptake.

To this end, we designed a reversed flow test, in which the specimen was vertically oriented such that the direction of water flow was aligned with gravity (i.e., downward). This contrasts with the original upward capillary absorption configuration. The experimental setup is illustrated in **Supplementary Figure 14a**.

If gravity were a significant factor, this alignment would be expected to accelerate water penetration or modify the characteristic shape of the uptake curve. However, as shown in the comparison of height-time profiles, no notable difference in water uptake height or rate was observed between the standard and downward configurations. The uptake curves were nearly identical throughout the test duration.

These results suggest that gravitational acceleration has limited to negligible impact on the capillary water absorption behavior in our experimental system. In particular, the characteristics of anomalous water uptake, such as the delayed inflection point and non-linear kinetics, appear independent of absorption direction.

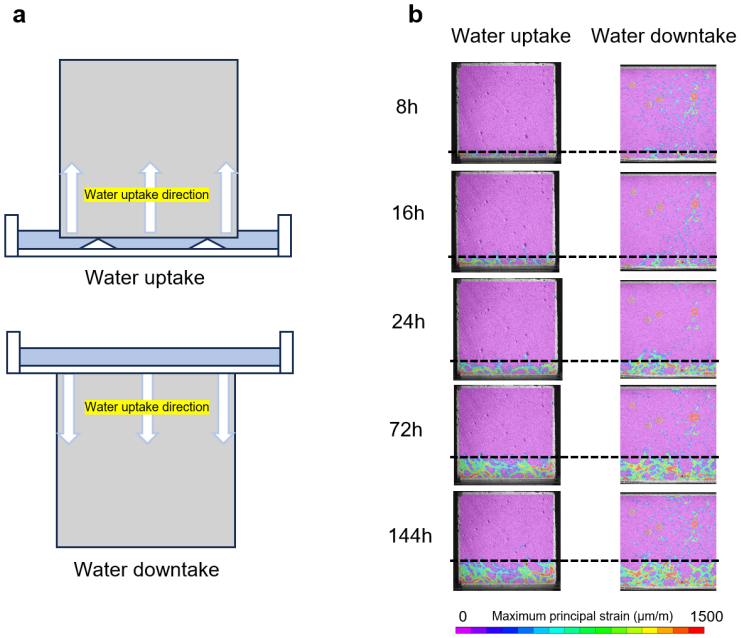

Supplementary Figure 14 Gravity has negligible influence on water absorption behavior in concrete specimens.
a Schematic illustration of the two experimental configurations: standard upward water uptake and downward "downtake" absorption, where the direction of water movement is aligned with gravity. Both setups maintain consistent sample geometry, sealing conditions, and water exposure depth.
b Comparison of vertical expansion height over time under the two configurations for samples dried at 20 °C. The results show no significant difference in deformation extent or rate, indicating that gravitational acceleration does not noticeably affect capillary absorption or swelling behavior in this system.

Supplementary Note 16. One-dimensional numerical simulation of swelling-induced water uptake

Background and purpose

The anomalous behavior of water uptake in cementitious materials cannot be accurately captured without considering two key mechanisms: (1) crack area evolution during wetting, as observed via digital image correlation (DIC), and (2) dynamic changes in pore structure, particularly the redistribution between capillary and fine pores, as revealed by ^{1}H-NMR. These coupled processes significantly alter the material's transport capacity and result in non-classical absorption dynamics.

In particular, the swelling of calcium–silicate–hydrate (C–S–H) phases plays a central role. The colloidal nature of C–S–H underlies both the volume change and the redistribution of water across multiscale pore domains. By altering the initial pore state via different drying conditions, we observed distinct behaviors in crack closure and retention evolution, suggesting that the anomalous uptake phenomenon is fundamentally driven by C–S–H swelling and its interaction with the evolving pore network.

To quantify these effects and validate our experimental interpretation, we developed a front-tracking one-dimensional simulation framework. The model integrates measured retention evolution, crack density, and region-specific diffusivity to reproduce the full trajectory of water front propagation. This numerical approach not only supports the physical mechanism inferred from in-situ observations but also enables predictive simulation under arbitrary initial conditions. It bridges the microscale pore evolution with macroscale transport anomalies, offering a unified platform for mechanistic understanding and material design optimization.

Governing equations and concepts

The fundamental concept stems from the **Lucas–Washburn equation**, which assumes that water imbibition in porous media follows a diffusion-like process. Under the classical assumption of constant diffusivity, the water front height h(t) is proportional to the square root of time:

$$h(\mathrm{t}) \propto \sqrt{\mathrm{t}}$$

However, for materials with evolving pore structure and spatially varying resistance, this relationship becomes more complex. We retain the form but adapt the propagation increment in each time step based on an effective diffusivity $D_{\mathrm{eff}}(\mathrm{t})$, such that:

$$h(\mathrm{t}) \approx 2 * \sqrt{D_{\mathrm{eff}}(\mathrm{t}) * \Delta \mathrm{t}}$$

Here, the factor 2 originates from the analytical solution to the classical diffusion equation. While its exact value is empirical and does not influence the core calculation logic, it provides a reasonable scaling for modeling purposes. Importantly, $D_{\mathrm{eff}}(\mathrm{t})$ is not constant, but recalculated at each step to capture the evolving resistance of the material.

We adopted the arithmetic average to calculate the effective diffusion coefficient $D_{\mathrm{eff}}(\mathrm{t})$. This choice is based on the assumption that each layer contributes proportionally to the overall water uptake. The arithmetic mean allows a better representation of the cumulative effects of structural evolution along the vertical profile, especially when the variation in $D(z,t)$ is gradually changing.

Hence, in this model, $D_{\mathrm{eff}}(\mathrm{t})$ is determined by averaging the layer-wise diffusion coefficients over the wetted depth $z_{\mathrm{front}}(t)$, see **Supplementary Figure 15a**.

$D_{\mathrm{eff}}(\mathrm{t})$ is the effective diffusion coefficient calculated from average value of layer-wise $D(z,t)$:

$$D_{\mathrm{eff}}(\mathrm{t}) = \sum_{0}^{z_{\mathrm{front}}} d\mathrm{z} \cdot D_{\mathrm{i}} \,/ z_{\mathrm{front}}$$

Then, the key challenge becomes determining the effective diffusivity $D_{\mathrm{eff}}(\mathrm{t})$ for each layer at any time, which requires a clear understanding of how $D_{\mathrm{eff}}(\mathrm{t})$ evolves with pore structure. In this study, we employ retention, defined as the ratio of the current capillary pore volume to the maximum volume (also can be written as $\theta_{\mathrm{t}}/\theta_{0}$, θ_{t} indicates the amount of water in the capillary or fine pores at time t, and θ_0 indicates the water content in that kind of

pore at the beginning of the C–S–H swelling-induced pore structure transformation, as shown in **Supplementary Figure 15b**). This parameter effectively captures the shrinkage of capillary channels due to C-S-H swelling. θ/θ_0 before pore transformation occurs is always 1. Afterward, it decreases linearly over time. We fitted and summarized them, as shown in **Supplementary Figure 15c**:

Then we introduce Poiseuille's Law to describe the relationship between channel's radius and diffusivity D. According to Poiseuille's Law, the volumetric flow rate Q of a liquid through a cylindrical capillary of radius r is proportional to the second power of the radius:

$$Q \propto r^2$$

This implies that larger pores dominate transport, and even small variations in radius can significantly change flow behavior. Since the diffusivity D in unsaturated porous systems can be analogized to effective mobility of water, it is also assumed to scale with pore radius as:

$$D(r) \propto r^n$$

Where n=2, which is common used in classical diffusion analogy, and it is what we use in this calculation

We generalize this as $D(r) \propto r^n$, and then relate pore radius to saturation, using a power-law form:

$$D \propto (\theta/\theta_0)^{\alpha}$$

where α=n/2=1, because retention is calculated based on the volume ratio, which under the cylindrical transmission channel assumption is the square of the aperture ratio. Then we get:

$$D(\mathrm{z},\mathrm{t}) = D_0 * (\frac{\theta(\mathrm{z},\mathrm{t})}{\theta_0})$$

Then, for capillary pores and fine pores, we respectively obtain:

$$D_{\mathrm{cap}}(\mathrm{z},\mathrm{t}) = D_0 * (\frac{\theta_{\mathrm{cap}}(\mathrm{z},\mathrm{t})}{\theta_{\mathrm{cap},0}})$$

$$D_{\mathrm{fine}}(\mathrm{z},\mathrm{t}) = D_0 * (\frac{\theta_{fine}(\mathrm{z},\mathrm{t})}{\theta_{\mathrm{fine},0}})$$

Since the proportion of initial capillary pores to small fine varies under different drying conditions, by determining the specific gravity of the initial transport channel based on the ratio of the area of capillary pores to small pores before the pore transformation begins as measured by NMR, the following can be obtained:

$$D(\mathrm{z},\mathrm{t}) = D_0 * \ (A_{\mathrm{cap},0} * \left(\frac{\theta_{\mathrm{cap}}(\mathrm{z},\mathrm{t})}{\theta_{\mathrm{cap},0}}\right) + A_{\mathrm{fine},0} * \left(\frac{\theta_{\mathrm{fine}}(\mathrm{z},\mathrm{t})}{\theta_{\mathrm{fine},0}}\right))$$

Furthermore, considering the closure of micro-cracks at the capillary pore scale, its influence on the tortuosity is significant and thus cannot be ignored. Therefore, a tortuosity coefficient constrained by $\frac{\theta_{cap}(z,t)}{\theta_{cap,0}}$ is added to the term of capillary pore transmission, and the equation is rewritten as:

$$D(\mathrm{z},\mathrm{t}) = D_0 * (\frac{A_{\mathrm{cap},0} * \left(\frac{\theta_{\mathrm{cap}}(\mathrm{z},\mathrm{t})}{\theta_{\mathrm{cap},0}}\right)}{\tau(\frac{\theta_{\mathrm{cap}}(\mathrm{z},\mathrm{t})}{\theta_{\mathrm{cap},0}})} + A_{\mathrm{fine},0} * \left(\frac{\theta_{\mathrm{fine}}(\mathrm{z},\mathrm{t})}{\theta_{\mathrm{fine},0}}\right))$$

The functional form of tortuosity remains an open question in current literature. In this study, we adopt an exponential formulation inspired by Archie's law[47] is employed here:

$$\tau\left(\frac{\theta_{\mathrm{cap}}(\mathrm{z},\mathrm{t})}{\theta_{\mathrm{cap},0}}\right) = \tau_0 * e^{(\beta*(1-\frac{\theta_{\mathrm{cap}}(\mathrm{z},\mathrm{t})}{\theta_{\mathrm{cap},0}}))}$$

It is known that there are aggregate areas, ITZ areas and mortar areas in the sample. In the observation of DIC, we have confirmed that there is a part of the crack accumulation area in the mortar area. Therefore, we can divide the concrete into four parts for treatment and determine their respective contributions to the transport according to the area proportion:

$$D_{\mathrm{total}}(\mathrm{z},\mathrm{t}) = A_{\mathrm{agg}} * D_{\mathrm{agg}} + A_{\mathrm{ITZ}} * D_{\mathrm{ITZ}} + A_{\mathrm{crack}} * D_{\mathrm{crack}} + A_{\mathrm{matrix}} * D_{\mathrm{matrix}}$$

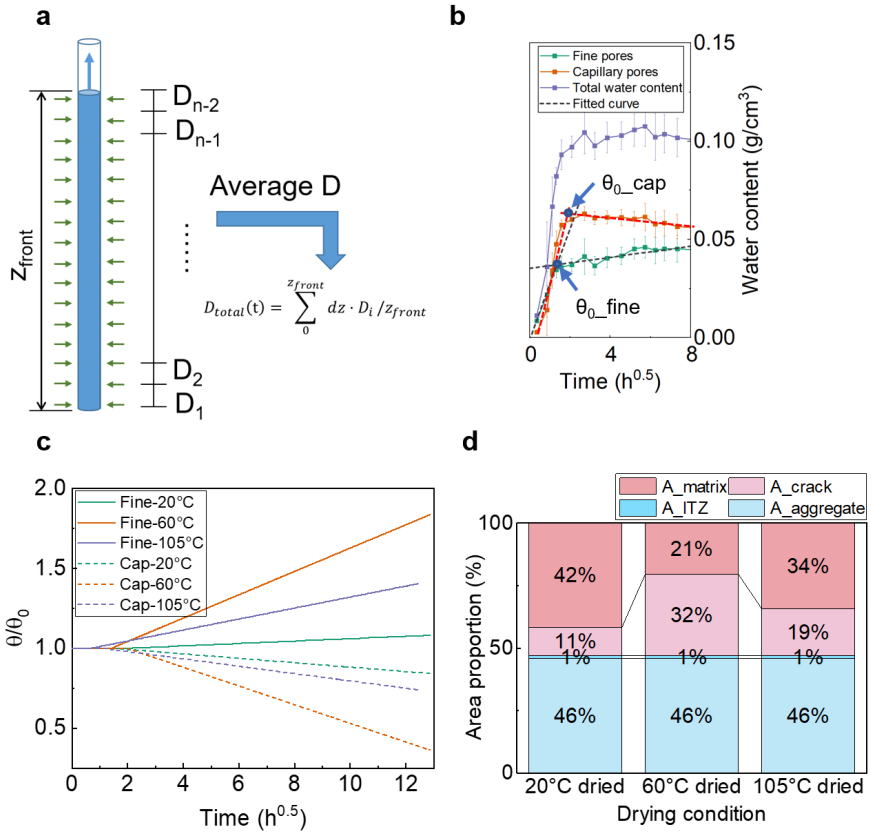

Supplementary Figure 15 Parameter extraction and structural input for the 1D swelling-induced transport model.

a Schematic of the layer-wise computation of the total effective diffusivity D_{total} used in the model. The diffusivity is averaged over the wetted depth z_{front} by summing the local values D_{i} weighted by their layer thickness dz. During water uptake, D_{i} and D_{total} are keeping changing.

b Example of NMR-derived pore-scale water content evolution used to determine the initial retention capacity ($\theta_{0,\mathrm{cap}}$, $\theta_{0,\mathrm{fine}}$). Separate contributions from capillary pores and fine pores are shown, and fitted curves are used to define input retention functions.

c Evolution of normalized retention θ_t/θ_0 for both capillary and fine pores under different drying conditions (20 °C, 60 °C, and 105 °C). These curves are used to dynamically update layer-wise diffusivity during simulation.

d DIC-derived area proportions of matrix, crack-rich zones, ITZ, and aggregates under the three drying regimes. These values define the spatial heterogeneity and regional weighting in the transport calculation.

The value of the parameters

Set of the value of the parameters was shown in **Supplementary Table 1**.

Supplementary Table 1. Materials and physical properties used in mix design.

Parameters	20°C	60°C	105°C	Notes	Data source
A_aggregate	0.460	0.460	0.460	Calculated from mix ratio	Calculated
A_crack	0.113	0.324	0.188	Calculated from DIC	Calculated

A_ITZ	0.005	0.005	0.005	Assuming ITZ thickness=20μm and r_Aggregate=5mm, calculated from Aggregate	Calculated
A_matrix	0.422	0.211	0.347	Calculated from DIC	Calculated
w_cap	0.9	0.9	0.9	Ratio of transport capacity of two kinds of pores was set as 9:1	Experiential
w_fine	0.1	0.1	0.1		
A_cap,0	0.2825	0.5116	0.5746	Area proportion of two kinds of pores in the initial state, calculated by NMR	Calculated
A_fine,0	0.7175	0.4884	0.4254		
τ_matrix_0	1	1	1	Tortuosity of sound matrix was set as 1	Experiential
τ_crack_0	0.2	0.15	0.1	Tortuosity of cracked area was set as 0.1-0.2, the ratio of 20, 60 and 105°C was 2: 1.5: 1	Experiential
β_matrix	4	4	4	β controls the sensitivity of Tortuosity to the change of θ/θ_0, which was set as 4	Experiential
β_crack	4	4	4		
k_ITZ	3	3	3	The increase multiple of the D_{ITZ} relative to D_{matrix}, set as 3	Experiential
k_exp	2.32	9.54	11.37	k-height, measured by the experiment	Calculated
D_0	12.3255	53.8227	63.8089	Calculated by k_exp	Calculated

Supplementary Note 17. Materials and experimental protocol

This section details the materials and experimental procedures used in this study. Samples with dimensions of 100×10×100 mm³ were used to explore the relationship between capillary water uptake height and mass change. Independent tests using DIC and X-CR were conducted to validate the spatial consistency between strain and moisture fields.

The pore and crack characterization based on BSE imaging was also conducted on specimens of the same dimensions. In addition, 50×50×100 mm³ specimens were used for single-sided H^1-NMR testing to investigate local water redistribution and pore-scale self-sealing behavior during absorption.

Supplementary Table 2. Materials and physical properties used in mix design.

Material	Notation	Properties
Water	W	Tap water
Cement	C	Ordinary Portland cement, density: 3.16g/cm3
Fine aggregate	S	Mountain sand, density at surface dry condition:2.58g/cm3, absorption:1.80%
Coarse aggregate	G	Crushed sandstone, density: 2.64g/cm3, absorption:0.69%, Solid volume proportion:59.1%

Agent	Ad	AE water reducing agent (Lignosulfonic and polycarboxylic acid type)
	AE	Air entraining agent (Resin acid series interfacial active compounds)

Note: Density and absorption data refer to surface-dry condition.

Supplementary Table 3. Mix proportions and fresh concrete properties.

W/C (%)	s/a (%)	Mass (kg/m^3)						Concrete volume fraction (m^3/m^2)	Temperature (°C)	Slump (cm)	Dispersion degree (mm)	Air content (%)
		W	C	S	G	Ad	AE					
55	47.5	165	300	851	964	2.25	0.0045	0.618	20	13.5	257×245	5

Note: W/C and s/a ratios by mass. s/a: sand-to-aggregate ratio

Supplementary Table 4. Sample grouping and test matrix under different drying conditions.

Drying condition	Sample size (mm^3)	Mass measurement	X-CR	DIC	BSE	Single-sided H1-NMR
20℃(15%RH)	100×10×100	√	√	√	√	
	50×50×100					√
60℃	100×10×100	√	√	√	√	
	50×50×100					√
105℃	100×10×100	√	√	√	√	
	50×50×100					√

Supplementary Appendices

Supplementary Appendix 1 The definition of the θ/θ_0 function

```
function [fine] = retention_fine_20(t)
% retention_cap_20
% The θ/θ0 of fine pores during the water uptake of the sample dried at 20°C
if t<=1.95
    fine=1;
else
    fine=0.00075*t+0.9853;
end
end

function [cap] = retention_cap_60(t)
% retention_cap_60
% The θ/θ0 of capillary pores during the water uptake of the sample dried at 60°C
if t<=1.97
    cap=1;
else
    cap=-0.0586*t+1.1156;
end
end

function [cap] = retention_cap_105(t)
% retention_cap_105
% The θ/θ0 of capillary pores during the water uptake of the sample dried at 105°C
if t<=1.12
    cap=1;
else
    cap=-0.023*t+1.0257;
end
end

function [fine] = retention_fine_20(t)
% retention_cap_20
% The θ/θ0 of fine pores during the water uptake of the sample dried at 20°C
if t<=1.95
    fine=1;
else
    fine=0.00075*t+0.9853;
end
end
```

```
function [fine] = retention_fine_60(t)
% retention_cap_60
% The θ/θ0 of fine pores during the water uptake of the sample dried at 60°C
if t<=1.46
    fine=1;
else
    fine=0.0731*t+0.8975;
end
end

function [fine] = retention_fine_105(t)
% retention_cap_105
% The θ/θ0 of fine pores during the water uptake of the sample dried at 105°C
if t<=0.66
    fine=1;
else
    fine=0.0344*t+0.9773;
    end
end
```

Supplementary Appendix 2 Calculate D_0 by fitting experimental water uptake height curve

```
function [Deff0,D0] = cal_D0(k_exp,A_aggregate, A_crack, A_ITZ,A_cap, A_fine, w_cap, w_fine,
tau_matrix_0, tau_crack_0)
%cal_D0
%
%% Calculate Deff0 and D0
% ----------------------
% Step one
% ----------------------
% We have already known:
% k = sqrt(Deff0) * A
% Normally A = 2    (adjustable)
A = 2;
% Fitting k to get effective D: Deff0
Deff0 = (k_exp / A)^2;        % unit: mm^2/h
% ----------------------
% Step two:
% ----------------------
% calculate area proportion
A_matrix=1-A_crack-A_aggregate-A_ITZ;
% The increase multiple of the DITZ relative to Dmatrix, set as 3
k_ITZ = 3;
```

```
% In the initial state, the expansion and transformation does not occur. Therefore, the tortuosity is only taken as the initial value
% Diffusion coefficients of each region (relative to D0)
D_matrix_rel = A_cap*w_cap/tau_matrix_0+A_fine*w_fine;
D_crack_rel = A_cap*w_cap/tau_crack_0+A_fine*w_fine;
D_aggregate_rel = 1e-6; % The aggregate is almost imtransportable
D_ITZ_rel = k_ITZ *D_matrix_rel;
% The relationship between Deff0 and D0:
% Deff0 = (Area_matrix*D_matrix_rel + Area_crack*D_crack_rel + Area_aggregate*D_aggregate_rel + Area_ITZ*D_ITZ_rel)* D0
% Get D0
D0 = Deff0/(A_matrix*D_matrix_rel + A_crack*D_crack_rel + A_aggregate*D_aggregate_rel + A_ITZ*D_ITZ_rel);
% ----------------------
% Finish, output
% ----------------------
% Deff0 is the initial effective diffusion coefficient obtained through experimental fitting
% D0 is the theoretical reference diffusion coefficient for the internal structure (used for subsequent regional modeling)
end
```

Supplementary Appendix 3 Calculate the water uptake height

```
function [height_history, Deff_history] = simulate_uptake( time_sqrt, D0, alpha, h_max, A_aggregate, A_crack, A_ITZ,beta_matrix, beta_crack, A_cap, A_fine, w_cap, w_fine, k_ITZ, tau_matrix_0, tau_crack_0,retention_cap,retention_fine)
% Notes of simulate_uptake
    num_steps = length(time_sqrt);
    height_history = zeros(num_steps, 1);          % simulated water front at each time
    Deff_history = zeros(num_steps, 1);             % record D values for plotting/debugging
    % Initial water front position
    front_z = 0.1;
    % Calculate the A_matrix
    A_matrix= 1-A_aggregate-A_crack-A_ITZ;
    % set the size of t0
    t0=zeros(num_steps,2);
    for i = 2:num_steps
        dt_sqrt = time_sqrt(i) - time_sqrt(i-1);
        % height of water front£¨unit: mm£©
        current_z = front_z;
        current_z = min(current_z, h_max);    % set the maximum height
        % Extract slices for the current water front region
        for ii=0:0.1:round(current_z,1) %the height resolution is 0.1 mm
            for k=1:length(time_sqrt)
```

```
            if   t0(k,1)>ii
                t0_cal(round(ii*10+1),1)=t0(k,2);
                break
             else
                t0_cal(round(ii*10+1),1)=0;
             end
        end
        % For each layer calculate the diffusion coefficient considering t-t0
        % transfer h0.5 to h, than minues, than transfer h to h0.5
        time_diff_save(round(ii*10+1),i)= sqrt(time_sqrt(i)^2 - t0_cal(round(ii*10+1),1)^2);
        time_diff= time_diff_save(round(ii*10+1),i);
        % calculate tau, D for every parts
        % retention(t) is a function to describe the change of ¦È/¦È0
    tau_matrix(round(ii*10+1),i)=tau_matrix_0*exp(beta_matrix*(1-retention_cap(time_diff)));
    tau_crack(round(ii*10+1),i)=tau_crack_0*exp(beta_crack*(1-retention_cap(time_diff)));
    D_matrix(round(ii*10+1),i) = D0 * (A_cap*w_cap*retention_cap(time_diff)^
alpha/tau_matrix(round(ii*10+1),i)+A_fine*w_fine*retention_fine(time_diff)^ alpha);   % Matrix
diffusion
    D_crack(round(ii*10+1),i)= D0 * (A_cap*w_cap*retention_cap(time_diff)^
alpha/tau_crack(round(ii*10+1),i)+A_fine*w_fine*retention_fine(time_diff)^ alpha);   % Crack
diffusion
    D_aggregate(round(ii*10+1),i) = 1e-6; % Aggregate diffusion
    D_ITZ(round(ii*10+1),i) =    k_ITZ * D_matrix(round(ii*10+1),i);    % ITZ diffusion
    % Combine these adjusted values using the respective weights
    D_eff(round(ii*10+1),i) = A_matrix * D_matrix(round(ii*10+1),i) + A_crack *
D_crack(round(ii*10+1),i) + A_aggregate * D_aggregate(round(ii*10+1),i) + A_ITZ *
D_ITZ(round(ii*10+1),i);
    D_layers(round(ii*10+1),i) = D_eff(round(ii*10+1),i);
    % Update t0 for layers that are now in contact with water
    t0(i,1) = current_z; % Initial contact at the first layer
    t0(i,2) = time_sqrt(i);
    end
    % Compute the harmonic average of all layer D values up to the current height
    D_total = mean(D_layers(:,i));
    % Store the computed D value for this time step
    Deff_history(i) = D_total;
    % Update water front height using ¡Ì(D)¡¤¦¤t
    dh = 2 * sqrt(D_total) * dt_sqrt;
    front_z = front_z + dh;
    % Limit the water front height to the maximum height
    if front_z > h_max
        front_z = h_max;
    end
```

```
            height_history(i) = front_z;
        end
    end
```

Supplementary Appendix 4 The main program used for execution

```
%load the .mat file containing all parameters
load('cal_transport.mat');
close all
% 'cal_D0'is a function to calculae the D0 by using k-height
% D0_20 mains D0 while Deff0_20 mains the effective D considering all parts
[Deff0_20,D0_20]=cal_D0(k_exp_20,Proportion_20(1,1), Proportion_20(2,1),
Proportion_20(3,1),A_pores_initial(1,1),A_pores_initial(2,1), w_cap, w_fine, tau_matrix_0,
tau_crack_0_20);
[Deff0_60,D0_60]=cal_D0(k_exp_60,Proportion_60(1,1), Proportion_60(2,1),
Proportion_60(3,1),A_pores_initial(1,2),A_pores_initial(2,2), w_cap, w_fine, tau_matrix_0,
tau_crack_0_60);
[Deff0_105,D0_105]=cal_D0(k_exp_105,Proportion_105(1,1), Proportion_105(2,1),
Proportion_105(3,1),A_pores_initial(1,3),A_pores_initial(2,3), w_cap, w_fine, tau_matrix_0,
tau_crack_0_105);
% 'simulate_uptake'is a function to calculae water uptake
[height_history_20, Deff_history_20]=simulate_uptake(t_20, D0_20, alpha, h_max,
Proportion_20(1,1), Proportion_20(2,1), Proportion_20(3,1), beta_matrix,
beta_crack_20,A_pores_initial(1,1),A_pores_initial(2,1),w_cap, w_fine, k_ITZ, tau_matrix_0,
tau_crack_0_20,@retention_cap_20,@retention_fine_20);
[height_history_60, Deff_history_60]=simulate_uptake(t_60, D0_60, alpha, h_max,
Proportion_60(1,1), Proportion_60(2,1), Proportion_60(3,1), beta_matrix,
beta_crack_60,A_pores_initial(1,2),A_pores_initial(2,2),w_cap, w_fine, k_ITZ, tau_matrix_0,
tau_crack_0_60,@retention_cap_60,@retention_fine_60);
[height_history_105, Deff_history_105]=simulate_uptake(t_105, D0_105, alpha, h_max,
Proportion_105(1,1), Proportion_105(2,1), Proportion_105(3,1), beta_matrix,
beta_crack_105,A_pores_initial(1,3),A_pores_initial(2,3), w_cap, w_fine, k_ITZ, tau_matrix_0,
tau_crack_0_105,@retention_cap_105,@retention_fine_105);
% draw the curves and compare them with experimental results
figure
plot(t_20,height_history_20,'b-','LineWidth',1.5);
hold on
scatter(exp_20(:,1),exp_20(:,2),'bo');
hold on
plot(t_60,height_history_60,'r-','LineWidth',1.5);
hold on
scatter(exp_60(:,1),exp_60(:,2),'ro');
hold on
plot(t_105,height_history_105,'g-','LineWidth',1.5);
hold on
```

```
scatter(exp_105(:,1),exp_105(:,2),'go');
hold off
legend('Simulated 20¡ãC', 'Experimental 20¡ãC','Simulated 60¡ãC', 'Experimental 60¡ãC', 'Simulated 105¡ãC', 'Experimental 105¡ãC', ...
    'Location', 'northwest');
xlabel('Time (h^{0.5})');
ylabel('Penetration Height (mm)');
title('Water Uptake Comparison');
grid on;
```

Supplementary references:

1. Parrott LJ. Water absorption in cover concrete. *Materials and Structures* **25**, 284-292 (1992).

2. Hall C. Water sorptivity of mortars and concretes: a review. *Magazine of Concrete Research - MAG CONCR RES* **41**, 51-61 (1989).

3. Wang X*, et al.* Influence of low vacuum and high temperature condition on moisture transport and dry shrinkage of mature concrete. *Journal of Building Engineering* **95**, (2024).

4. Zhang G, Li Z, Zhang L, Shang Y, Wang H. Experimental research on drying control condition with minimal effect on concrete strength. *Construction and Building Materials* **135**, 194-202 (2017).

5. Ren F, Zhou C, Zeng Q, Zhang Z, Angst U, Wang W. Quantifying the anomalous water absorption behavior of cement mortar in view of its physical sensitivity to water. *Cement and Concrete Research* **143**, (2021).

6. Andrade C, Saucedo L, Rebolledo N, Cabeza S, Meinel D. X-Ray computed tomography and traditional analysis of a capillary absorption test in cement pastes. *Cement and Concrete Composites* **113**, (2020).

7. Alderete NM, Villagrán Zaccardi YA, De Belie N. Physical evidence of swelling as the cause of anomalous capillary water uptake by cementitious materials. *Cement and Concrete Research* **120**, 256-266 (2019).

8. Alderete N*, et al.* Capillary imbibition in mortars with natural pozzolan, limestone powder and slag evaluated through neutron radiography, electrical conductivity, and gravimetric analysis. *Cement and Concrete Research* **118**, 57-68 (2019).

9. Roels S, Carmeliet J. Analysis of moisture flow in porous materials using microfocus X-ray radiography. *International Journal of Heat and Mass Transfer* **49**, 4762-4772 (2006).

10. Cheng L*, et al.* Plugging effect of fine pore water in OPC and LC3 paste during accelerated carbonation monitored via single-sided nuclear magnetic resonance spectroscopy. *Cement and Concrete Research* **186**, (2024).

11. Li J*, et al.* Longitudinal single-sided NMR study: Silica-to-alumina ratio changes the reaction mechanism of geopolymer. *Cement and Concrete Research* **160**, (2022).

12. Glawe C, Georget F, Raupach M, Matschei T. Multi technique characterization of the carbonation affected zone including non-destructive single sided 1H NMR. *Cement and Concrete Research* **178**, (2024).

13. Long Z, Zhang Z, Zhang H. Closure to "Nondestructive measurement of the capillary water absorption coefficient and water transport behaviors of porous building materials by using single-sided NMR". *Construction and Building Materials* **433**, (2024).

14. Janssen H. Discussion of "Nondestructive measurement of the capillary water absorption coefficient and water transport behaviors of porous building materials by using single-sided NMR". *Construction and Building Materials* **433**, 136378 (2024).

15. Maruyama I, Ohkubo T, Haji T, Kurihara R. Dynamic microstructural evolution of hardened cement paste during first drying monitored by 1H NMR relaxometry. *Cement and Concrete Research* **122**, 107-117 (2019).

16. Muller ACA, Mitchell J, McDonald PJ. Proton nuclear magnetic resonance relaxometry. *A Practical Guide to Microstructural Analysis of Cementitious Materials*, (2018).

17. Muller ACA, Scrivener KL, Gajewicz AM, McDonald PJ. Densification of C–S–H Measured by 1H NMR Relaxometry. *The Journal of Physical Chemistry C* **117**, 403-412 (2013).

18. Gajewicz-Jaromin AM, McDonald PJ, Muller ACA, Scrivener KL. Influence of curing temperature on cement paste microstructure measured by 1H NMR relaxometry. *Cement and Concrete Research* **122**, 147-156 (2019).

19. McDonald PJ, Istok O, Janota M, Gajewicz-Jaromin AM, Faux DA. Sorption, anomalous water transport and dynamic porosity in cement paste: A spatially localised 1H NMR relaxation study and a proposed mechanism. *Cement and Concrete Research* **133**, (2020).

20. Maruyama I, Nishioka Y, Igarashi G, Matsui K. Microstructural and bulk property

changes in hardened cement paste during the first drying process. *Cement and Concrete Research* **58**, 20-34 (2014).

21. Soja W, Georget F, Maraghechi H, Scrivener K. Evolution of microstructural changes in cement paste during environmental drying. *Cement and Concrete Research* **134**, (2020).

22. Yim HJ, Kim JH, Park S-J, Kwak H-G. Characterization of thermally damaged concrete using a nonlinear ultrasonic method. *Cement and Concrete Research* **42**, 1438-1446 (2012).

23. Maruyama I, Sasano H, Nishioka Y, Igarashi G. Strength and Young's modulus change in concrete due to long-term drying and heating up to 90°C. *Cement and Concrete Research* **66**, 48-63 (2014).

24. Hou S, Li K, Wu Z, Li F, Shi C. Quantitative evaluation on self-healing capacity of cracked concrete by water permeability test – A review. *Cement and Concrete Composites* **127**, (2022).

25. Litorowicz A. Identification and quantification of cracks in concrete by optical fluorescent microscopy. *Cement and Concrete Research* **36**, 1508-1515 (2006).

26. Maruyama I, Sasano H, Lin M. Impact of aggregate properties on the development of shrinkage-induced cracking in concrete under restraint conditions. *Cement and Concrete Research* **85**, 82-101 (2016).

27. Zhang P, Wittmann FH, Zhao T, Lehmann EH. Neutron imaging of water penetration into cracked steel reinforced concrete. *Physica B: Condensed Matter* **405**, 1866-1871 (2010).

28. Zhang P, Wittmann FH, Zhao T-j, Lehmann EH, Vontobel P. Neutron radiography, a powerful method to determine time-dependent moisture distributions in concrete. *Nuclear Engineering and Design* **241**, 4758-4766 (2011).

29. Van Belleghem B*, et al.* Capillary water absorption in cracked and uncracked mortar – A comparison between experimental study and finite element analysis. *Construction and Building Materials* **110**, 154-162 (2016).

30. Schröfl C, Mechtcherine V, Kaestner A, Vontobel P, Hovind J, Lehmann E. Transport of water through strain-hardening cement-based composite (SHCC) applied on top of cracked reinforced concrete slabs with and without hydrophobization of cracks – Investigation by neutron radiography. *Construction and Building Materials* **76**, 70-86 (2015).

31. Wilson MA, Hoff WD, Hall C. Water movement in porous building materials—X. Absorption from a small cylindrical cavity. *Building and Environment* **26**, 143-152 (1991).

32. Bernadiner MG. A capillary microstructure of the wetting front. *Transport in Porous Media* **30**, 251-265 (1998).

33. Lee HK, Lee KM, Kim YH, Yim H, Bae DB. Ultrasonic in-situ monitoring of setting process of high-performance concrete. *Cement and Concrete Research* **34**, 631-640 (2004).

34. Hanžič L, Ilić R. Relationship between liquid sorptivity and capillarity in concrete. *Cement and Concrete Research* **33**, 1385-1388 (2003).

35. Hanžič L, Kosec L, Anžel I. Capillary absorption in concrete and the Lucas–Washburn equation. *Cement and Concrete Composites* **32**, 84-91 (2010).

36. Zhang Z, Angst U. Different anomalies of two-stage water absorption in carbonated and non-carbonated cement-based materials. *Cement and Concrete Research* **183**, (2024).

37. Khanzadeh Moradllo M, Qiao C, Hall H, Ley MT, Reese SR, Weiss WJ. Quantifying fluid filling of the air voids in air entrained concrete using neutron radiography. *Cement and Concrete Composites* **104**, (2019).

38. Alderete NM, Villagrán Zaccardi YA, De Belie N. Mechanism of long-term capillary water uptake in cementitious materials. *Cement and Concrete Composites* **106**, (2020).

39. Hall C. Anomalous diffusion in unsaturated flow: Fact or fiction? *Cement and Concrete Research* **37**, 378-385 (2007).

40. Boltzmann L. Zur Integration der Diffusionsgleichung bei variabeln Diffusionscoefficienten. *Annalen der Physik* **289**, 959-964 (1894).

41. Matano C. On the Relation between the Diffusion-Coefficients and Concentrations of Solid Metals (The Nickel-Copper System). *Japanese Journal of Physics* **8**, (1933).

42. Kanematsu M, Tsuchiya N, Noguchi T. Fundamental research on isotherm capillary absorption of concrete by neutron radiography. *Journal of Structural and Construction Engineering (Transactions of AIJ)* **78**, 1339-1347 (2013).

43. Gummerson RJ, Hall C, Hoff WD, Hawkes R, Holland GN, Moore WS. Unsaturated water flow within porous materials observed by NMR imaging. *Nature* **281**, 56-57 (1979).

44. Villagrán Zaccardi YA, Alderete NM, De Belie N. Improved model for capillary absorption in cementitious materials: Progress over the fourth root of time. *Cement and Concrete Research* **100**, 153-165 (2017).

45. Xiao J, Cai J, Xu J. Saturated imbibition under the influence of gravity and geometry. *J Colloid Interface Sci* **521**, 226-231 (2018).

46. Fries N, Dreyer M. An analytic solution of capillary rise restrained by gravity. *Journal of Colloid and Interface Science* **320**, 259-263 (2008).

47. Glover PWJ. A new theoretical interpretation of Archie's saturation exponent. *Solid Earth Discussions* **8**, 1-10 (2017).